Research paper

Simulation-based process optimization of laser-based powder bed fusion by means of beam shaping

Constantin Zenz [a],[*],[1], Michele Buttazzoni [a],[1], Mario Martínez Ceniceros [b],
Rodrigo Gómez Vázquez [a], Jose Ramón Blasco Puchades [b], Luis Portolés Griñán [b], Andreas Otto [a]

[a] Institute of Production Engineering and Photonic Technologies, TU Wien, Getreidemarkt 9, 1060 Wien, Austria
[b] AIDIMME, Leonardo da Vinci 38, 46980, Paterna, Spain

ABSTRACT

Laser powder bed fusion of metals (PBF-LB/M) is an additive manufacturing technique which has recently been growing in popularity in industrial use cases. However, several challenges persist, including the issue of solidification cracking observed in widely used Ni-based superalloys. Through retrofitting an existing PBF machine with a dual beam system capable of dynamic beam shaping, it is possible to overcome this issue. The appropriate process parameters for the laser beam need to be determined prior to manufacturing the system. In this regard we propose a methodology that utilizes a numerical simulation tool to identify optimized parameters. To demonstrate the effectiveness of this approach, two example processes are presented. Initially the numerical model is validated by comparing its results against experimental data obtained from single track scans of two metal powders, CM247LC and IN713LC. Subsequently, an optimization study is conducted to identify optimal combinations of differently shaped and sized primary and secondary beams. The goal is to reduce the cooling rates within certain critical temperature ranges, thus mitigating the likelihood of solidification cracking, while avoiding the occurrence of other process defects such as balling, porosity, or lack of fusion. The effectiveness of these beam shapes is then verified through the production of physical samples. Through this example, a methodology for leveraging physics-based, model-driven process optimization is presented. Additionally, insights into the potential application of the same model for large-scale simulations are provided.

1. Introduction

Additive manufacturing (AM) has revolutionized production by allowing the creation of complex shapes directly from three-dimensional CAD models. Initially utilized primarily for non-functional design prototypes (rapid prototyping), the numerous advantages of AM over conventional processes, have led to its rapid adoption across various industries, including aerospace, automotive, medical and energy [1]. These benefits encompass the ability to fabricate customized parts, minimize material waste and manufacture shapes, that were previously unattainable using conventional manufacturing techniques [2]. The industry's adoption of AM has been made possible by advancements in high-power industrial lasers and the development of new metal powders over the past two decades [1]. PBF-LB/M is a manufacturing process that involves dividing a three-dimensional geometry into multiple layers, each with a predetermined layer height, which are subsequently manufactured. To build each layer, a metal powder is evenly spread across a substrate, which can be either a plate or a previously processed powder layer. Utilizing a laser beam, the powder is selectively melted to construct the geometry of a single layer. Subsequent re-solidification of the molten metal gives the required shape. This process is repeated for each layer, with the build plate being lowered and a new layer of powder applied afterwards. While AM techniques are applied to various types of materials, most research and development has been concentrated in the domain of metal AM. Recent research efforts are focused on the development of new materials, as well as process optimization, including the development of scanning strategies for the reduction of residual stresses and improvement of part properties [2]. As noted by DebRoy et al. [3], most research published on metal AM covers fundamentals and lacks direct relevance

for practical applications, whereas industrially exploitable research activities are mostly performed by corporations and therefore remain unpublished. This leaves a research gap in the area of applied research on AM.

During the project CUSTODIAN [4], funded by the European Union, a novel methodology for enhancing established industrial processes through laser beam shaping was developed. Within this approach, new or existing machines are equipped with a laser head containing a passive optical element, facilitating dynamic freeform beam shaping on the basis of Multi Plane Light Conversion (MPLC) [5]. The main advantages of this technology are the complete freedom of beam shape design and the possibility of retrofitting any existing machine. However, one limitation of this technology is that the desired beam shape, which can then be dynamically modulated to a certain extent, must be known prior to manufacturing the device. Therefore, the beam shapes cannot be found experimentally and physics-based simulations are used instead. A similar use case for the optimization of beam shapes in a laser beam welding process has previously been presented by Buttazzoni et al. [6].

This work showcases the applicability of this method to PBF-LB/M processes. It demonstrates the utilization of an MPLC device to add a secondary laser beam to a process where crack-free parts cannot be achieved using a single Gaussian laser beam. Two widely used nickel-based alloys, CM247LC and IN713LC, were selected as suitable materials for this optimization study based on their industrial significance and inherent susceptibility to cracking. The simulation model is used to obtain preliminary beam shapes with the aim of reducing cooling rates and thus crack susceptibility, while avoiding the occurrence of other process defects.

In contrast to welding, where information on weldability and suitable process parameters for various alloys is widely available, information on printability and suitable parameter spaces for AM processes is scarce and correct process parameters are often obtained through trial-and-error experiments [1]. This lack of process understanding calls for accurate, physics-based, models to gain a better understanding and to use these models as process optimization tools [7,8]. Many transient phenomena occurring in PBF-LB/M processes are only directly observable, when using very elaborate experimental setups [7]. For example, Cunningham et al. recently used high speed X-ray imaging techniques to perform in-situ observations of keyhole dynamics in PBF-LB/M [9]. While such methods are crucial in gaining process understanding and developing process models, they often fall short when it comes to industrial application, particularly in tasks like process optimization, where parameter studies have to be completed within a given time frame. A recent study conducted by Shu et al. [10] emphasized the importance of accurately incorporating convective heat- and mass transfer needs in a PBF-LB/M model. It was demonstrated that neglecting these factors can lead to inaccurate three-dimensional weld bead shape, even when a model has been validated by comparing two-dimensional cross sections to experiments. Hence, when employing a calibrated and validated model for straightforward optimization tasks that do not necessitate gaining further process insights, it is imperative to incorporate a certain level of complexity. Specifically it should always account for convective transport, considering the influence of surface tension-, recoil pressure- and buoyancy-induced forces. Simulation models can be characterized by the length scale on which they are applicable [7]. The model applied within this study is of the meso-scale type, where the fluid flow within the melt pool of each single process track is fully resolved, while also allowing the simulation of several layers, each consisting of several tracks, within reasonable amount of computing time (in the order of days on a desktop computer).

The present study aims at using physics-based simulations to improve a PBF-LB/M process via freeform beam shaping, enabled by MPLC technology. The effectiveness of the proposed methodology is tested at the example of reducing hot cracking susceptibility of

Nickel-based superalloys during PBF-LB/M by adding a secondary low-intensity heat source that reduces cooling rates while minimizing the occurrence of other process defects. The optimized beam shapes are realized by manufacturing a suitable MPLC device, which is then tested experimentally with the intention of fabricating dense parts with near-zero crack occurrence.

2. Simulation model

2.1. Model overview

The model utilized in this study was originally developed over a decade ago [11] to simulate the multiphysical problem of laser beam welding. Since then, it has been significantly expanded to encompass various laser-assisted manufacturing processes. The model has been used in various applications, such as simulating humping and the transition to cutting in laser beam welding of thin stainless steel foils [12], investigating spiking and pore formation in welding of copper and aluminum [13], exploring welding of dissimilar materials [14] and optimizing overlap welding of stainless steel sheets with a gap using MPLC technology [6]. Furthermore, laser cutting [15], and laser-based direct energy deposition [16] have been simulated. Additionally, the model is applicable to processes involving short pulsed lasers, such as ablation of multi-material structures using ns-pulses [17], and the processing of semiconductor materials [18] and dielectric materials [19] using ps- to fs-pulses.

The model is implemented using the open source C++ library Open-FOAM [20] and is based on the solver `multiphaseInterFoam`, an extension of the two-phase Volume-of-Fluid solver `interFoam` [21], capable of handling an arbitrary number of phases. Details on the model can be found in the aforementioned publications, especially [6, 12], as well as in [22]. A more in-depth description of the modeling approach is the topic of a forthcoming publication. Therefore, only a brief overview will be given here, with emphasis on process-specific details relevant for the simulation of PBF-LB/M. The steps performed within each time step of the simulation model are provided in Fig. 1 in the form of a flow chart and described below.

Caustic-aware laser beam propagation is modeled through a radiative transfer equation in combination with a ray tracing algorithm to account for multiple reflections. Reflectivity, R, is modeled through the Fresnel equations,

$$R_S = \left| \frac{cos(\beta) - \underline{n}\sqrt{1 - sin^2(\beta)/\underline{n}}}{cos(\beta) + \underline{n}\sqrt{1 - sin^2(\beta)/\underline{n}}} \right|, \tag{1}$$

$$R_P = \left| \frac{\underline{n}cos(\beta) - \sqrt{1 - sin^2(\beta)/\underline{n}}}{\underline{n}cos(\beta) + \sqrt{1 - sin^2(\beta)/\underline{n}}} \right|, \tag{2}$$

$$R = \frac{R_S + R_P}{2}, \tag{3}$$

where β is the local angle of incidence and $\underline{n}$ is the material's complex refractive index. Absorption of laser intensity I along its optical path, z, is modeled via Beer's law [23],

$$I(z) = I(0)\exp(-\kappa z), \tag{4}$$

with κ denoting the imaginary part of the material's complex refractive index, i.e., its extinction coefficient. Phase changes issue mass- and energy transfer between the respective phases. While melting and solidification are calculated through an enthalpy-porosity method [24], evaporation and condensation are modeled through the Hertz-Knudsen equation [25],

$$\frac{d\rho_{vap}}{dt} = \frac{1}{\Delta x}\sqrt{\frac{M}{2\pi RT}}\left(p_{sat} - p\right), \tag{5}$$

with ρ_{vap} denoting the mass density of the vapor phase, and p and T denoting pressure and temperature, respectively. Furthermore, R, M,
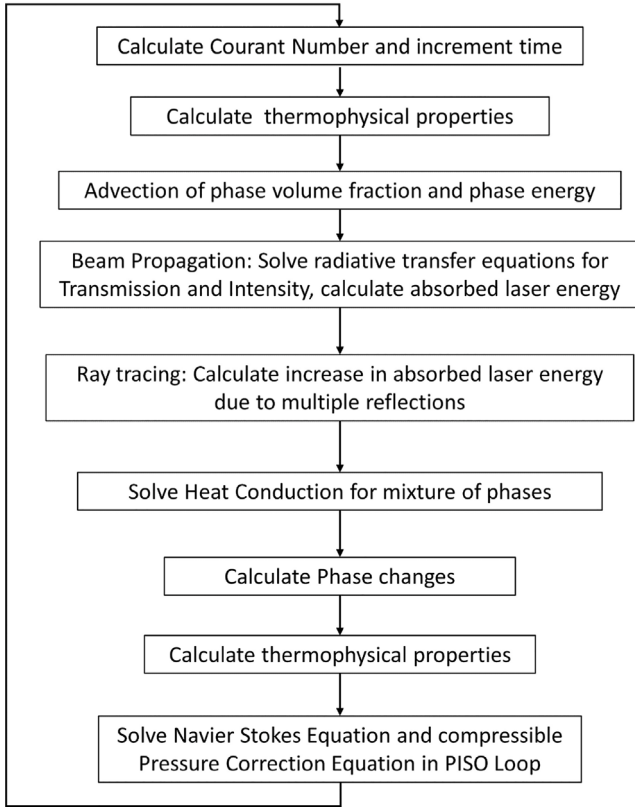
Fig. 1. Basic overview of calculation steps performed by the solver during each simulation time step.

and Δx denote the universal gas constant, the phase's molar mass and the local cell length, respectively. The local saturation pressure, p_{sat}, is calculated according to the Clausius–Clapeyron equation [26] as

$$p_{sat}(T) = p_{ref} \exp\left(\frac{ML}{T_b R}\left(1 - \frac{T_b}{T}\right)\right), \qquad (6)$$

with T_b and L denoting the phase's boiling temperature and latent heat of vaporization, respectively. Fluid flow is modeled through the Navier–Stokes equations in a homogeneous equilibrium mixture formulation as

$$\frac{\partial (\rho \boldsymbol{u})}{\partial t} + \nabla \cdot (\rho \boldsymbol{u}\boldsymbol{u}) = -\nabla p + \nabla \cdot \boldsymbol{\tau} - \boldsymbol{S_B} + \boldsymbol{S_S} + \boldsymbol{S_D}, \qquad (7)$$

where $\boldsymbol{u}$ is the velocity of the mixture of phases, and $\boldsymbol{\tau}$ is the viscous stress tensor, assuming laminar flow. The last three source terms on the right hand side of Eq. (7) contain body forces due to gravity, surface forces due to surface tension, and a source term for movement restriction in solid regions following Darcy's law, respectively. The Darcy term, $\boldsymbol{S_D}$, is modeled following the Carman–Kozeny equation [27] in the form

$$\boldsymbol{S_D} = -\frac{\mu}{A_{perm}} \frac{(\alpha_{solid})^2}{(1 - \alpha_{solid})^3 + 10^{-6}} \boldsymbol{u}, \qquad (8)$$

where α_{solid} is the volume fraction of solid material and μ is the dynamic viscosity of the mixture. The permeability area is set to $A_{perm} = 10^{-12}$ m^2. Temperature-dependent surface tension forces are explicitly included through $\boldsymbol{S_S}$, which is calculated as

$$\boldsymbol{S_S} = \sum_{i,j \forall i \neq j} \nabla \cdot \left[\sigma_{i,j} \left(\alpha_j \nabla \alpha_i - \alpha_i \nabla \alpha_j \right) \right], \qquad (9)$$

with surface energies $\sigma_{i,j}$ at interfaces between phase i and phase j, are calculated from the individual phase surface energies σ_i and σ_j, as [28]

$$\sigma_{i,j} = \sigma_i + \sigma_j - 2\sqrt{\sigma_i \sigma_j}. \qquad (10)$$

Body forces stemming from buoyancy are incorporated in the term $\boldsymbol{S_B}$. Forces resulting from recoil pressure due to evaporation are taken into account implicitly, as both liquid as well as vapor phases are treated as compressible fluids and a phase change from liquid to vapor issues a corresponding change in density resulting in expansion of the evaporating material, which in turn issues the recoil pressure.

Although a coupled CFD-DEM model taking into account individual powder particles was developed [16,29], the powder is modeled as a continuum, by introducing an additional, distinct Volume-of-Fluid phase for the powder to avoid the computational costs of modeling individual powder particles. This simplification is justified, as the powder properties and the powder spreading process are not part of the process parameters that are to be optimized, and, as also noted by Chen et al. [30], coupled CFD-DEM models currently lack the computational efficiency to be employed for industrial-scale processes. Therefore, the coupled CFD-DEM model was omitted in favor of computational efficiency. The characteristics of powder (low density, low thermal conductivity, high laser beam absorptivity) are considered through the respective material properties of the powder phase. It has been modeled as having 50% of the density of the bulk material, in accordance with conducted measurements, and its thermal conductivity was calculated in accordance with the model of Sih and Barlow [31], yielding a value of $\approx 2\%$ of the bulk material's conductivity. The employment of a pure continuum model introduces some limitations to the simulation model, e.g., the inability to account for the influence of particle shapes, sizes and packing densities, simplifications in the laser absorption behavior of the powder, and the inability to model powder-related phenomena such as denudation [30].

The simulation domain, spatial discretization and phase distribution at the start of a simulation are shown in Fig. 2. Mesh refinement was kept constant throughout the simulation and each subsequent run for consistency, where the cell size ranges from 25 μm up to 100 μm. At the boundaries different boundary conditions are applied. The boundary of the region depicted as solely containing surrounding phase in Fig. 2 is treated as an open boundary, facilitating the in- and outflow. Conversely, the remaining regions are treated as closed boundaries, eliminating the transfer of heat and mass across those boundaries. Heat accumulation effects were negligible as earlier tests showed.

2.2. Model validation

Experimental validation of mechanistic models is important as through each physical model, as well as through spatial and temporal discretization, some degree of uncertainty is introduced [7]. In order to gain physically accurate and practically relevant results, basic material properties were obtained from literature [32]. Data about the complex refractive index and the surface energies of all phases at high temperatures is scarce, due to the difficulty related to their measurement. Values for surface energies for instance are highly temperature-dependant as well as a function of physical state (solid, liquid, vapor) and alloy composition. These values are furthermore very sensitive to impurities. As these parameters have a great influence on the process outcome, great care was taken by properly calibrating it against experimental data. A summary of the properties for both investigated materials is provided in Appendix, in Figs. A.24 and A.25, respectively, and their chemical composition is listed in Table A.4.

Due to the fast convergence to a quasi-steady state process and the high computational cost associated with multi-track and multi-layer simulations, a single track was compared against experimental results in the calibration phase. The experiments used for the validation were performed at the facilities of AIDIMME, where the samples were also processed to produce cross sectional images that could then be compared against simulation results. All the tests presented in this publication have been conducted on a Concept Laser M3 PBF-LB/M machine, which has been modified with a high power laser (4000 W) and a custom scanning head housing the MPLC. This modification
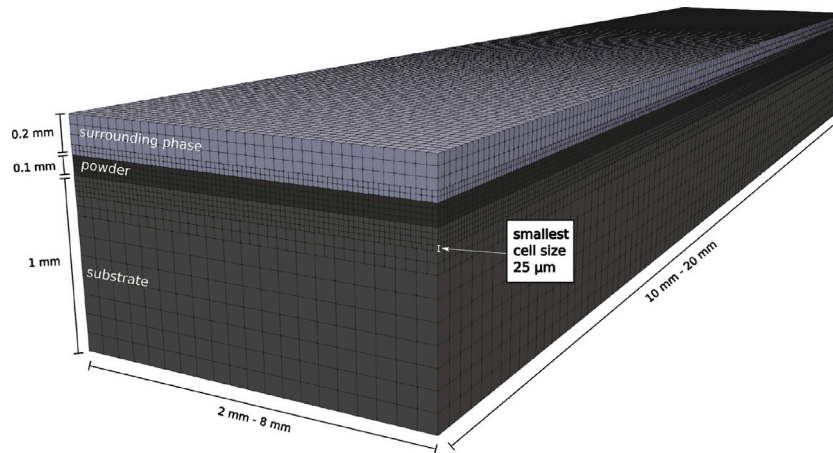
Fig. 2. Sketch of simulation domain used. Length and width are varied according to secondary beam size (the smallest domain is shown).
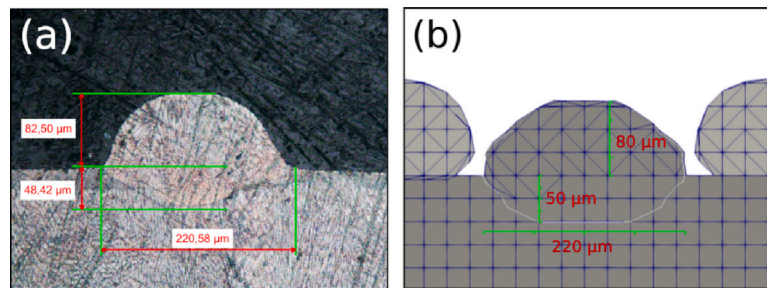

Fig. 3. Validation against experiment for CM247LC: (a) Experimental cross section. (b) Cross section resulting from the simulation.

Table 1
Single-beam process conditions for both investigated alloys used for validation of the simulation model.

	CM247LC	IN713LC
Scanning speed (mm/s)	750	750
Laser power (W)	452	520
Laser wavelength (nm)	1070	1070
Laser M^2	1	1
Laser focus position	on surface	on surface
Laser radius on substrate (µm)	176	176
Scan track length (mm)	9.5	9.5
Powder bed height (µm)	100	100

was required to deliver sufficient energy for both melting the scan tracks with a primary beam and heating the surrounding area with a secondary beam. A track of approx. 9.5 mm in length was scanned on a substrate immersed in powder with a layer height of 100 µm. A summary of the process parameters is presented in Table 1 for both materials. These were chosen after extensive experimental testing, where scanning speed and lasing power was varied between 300–800 mm/s and 200–600 W respectively. The chosen reference condition presents the highest part density and lowest crack appearance for each material. Samples presented in Figs. 3 and 4 were carried out with a standard Gaussian distribution beam shape. The validated simulation results can be seen in Fig. 3 for CM247LC and in Fig. 4 for IN713LC, respectively.

The decision to employ such a detailed and complex multiphysical model as an optimization tool was not only driven by the need to investigate the beam configuration's influence on cooling rates, but to also simultaneously identify (and avoid) any unwanted printing errors during the optimization process. This capability is shown here by example of the so-called balling defect. A first round of testing was carried out using the same laser power of 452 W for both investigated

alloys. The experimental results of three single tracks produced side-by-side by scanning IN713LC powder can be seen in Figs. 5 and 6, where three exemplary cross sectional views and a top view are provided respectively. It is noticeable, that balling occurred, where the liquid metal tends to agglomerate rather than to wet the underlying substrate. These conditions lead to the formation of melt spheres with high contact angles, exhibiting poor penetration of the substrate and a weld of unconnected sphere-like beads [33]. This surface tension force-driven phenomenon is usually associated with the Plateau–Rayleigh capillary instability [34]. Further proving the adaptability and accuracy of the here presented model, a simulation of this process condition was carried out and is provided in Fig. 7. The calculation and material properties used are the same as in the validation case (cf. Table 1), except for the lower input laser power. The formation mechanism behind the characteristic weld beads of unconnected, spherical structures shown in Figs. 6 and 7 can also be observed in the simulation, which is shown in Fig. 8, where the effect of evaporation-induced recoil pressure was deliberately excluded from the simulation to clearly show that this is a purely surface-tension driven phenomenon (as opposed to the humping mechanism, which could lead to a similar weld bead). The melt pool at the beginning of the process is very shallow and has a flat interface to the underlying colder substrate. Due to the low thermal conductivity of the surrounding inert gas and powder, most of the heat is dissipated downwards into the bulk material. Due to the larger temperature gradient at the bottom of the melt pool, more cooling takes place in this region and thus the top remains liquid for longer time and heat accumulates in this region. Because of the inverse relationship between surface tension and temperature, the resulting force will cause a contraction (inwards-pointing force) of the melt pool, pushing it into the characteristic spherical shapes. The phenomenon is further amplified, as the formation of spherical melt structures inhibits cooling and promotes heat accumulation (a). The surface tension force holding together the melt agglomeration drags the liquid along with
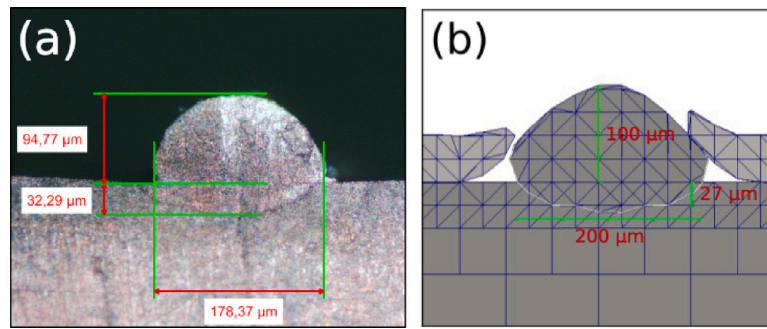
Fig. 4. Validation against experiment for IN713LC: (a) Experimental cross section. (b) Cross section resulting from the simulation.
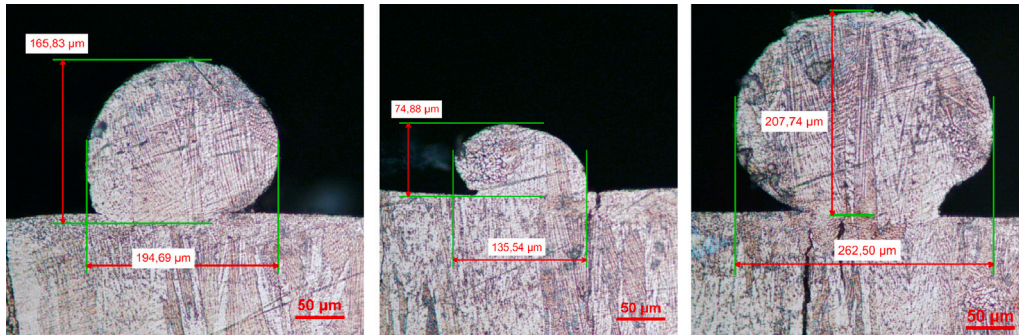

Fig. 5. Cross sectional views of single track experiments with IN713LC, laser power P = 452 W, scanning velocity v_s = 750 $\frac{mm}{s}$, hatch distance d_h = 100 μm and powder thickness t_p = 50 μm.

the moving heat source (b). After some time, the sphere solidifies from below, slowly halting the movement of the bead (c) and causing the first sphere to separate from the remaining melt pool (d). Its surface tension is now providing a force acting across the liquid bridge between the first and second sphere (d), also preventing the second sphere from moving. After complete separation has occurred and with increased accumulated heat input, the laser effectively penetrates the substrate, resulting in a larger shared interface between the melt pool and the substrate. Thus, in turn, creating a multidirectional (as opposed to only vertical) heat sink, mitigating the heat accumulation at the top of the weld bead that leads to the aforementioned phenomenon (e–f). The process now reaches a steady state with subsequently forming spheres not being dragged along and remaining smaller than the first one, leading to a periodic distribution of spherical structures (cf. top view in Fig. 7). The steady state exhibits the typical (idealized) phenomenon associated with Plateau–Rayleigh capillary instability [34].

In a similar way, other process defects could potentially be identified, e.g., the model was recently used to simulate pore formation [6]. Another example is the unwanted phenomenon of spatter [35], which could also be predicted by the model, as both the dynamics of metal vapor and shielding gas and the associated entrainment of liquid are fully resolved. However, given the low depth-to-width ratio of the investigated process, and therefore the absence of a keyhole (merely a mild vapor depression is present), spatter only plays a minor role.

3. Parameter study and beam shape optimization

A major issue in additive manufacturing of nickel-based superalloys is the appearance of cracks induced by thermal stresses during solidification in the final part. The high susceptibility to solidification cracking is associated with the high amount of Al and Ti within the alloys. According to [36], Ni-based superalloys are classified as non-weldable when exhibiting concentrations of Al and Ti above 6% wt., as is the case with both CM247LC and IN713LC. Non-weldability can be taken as a measure of non-printability in this context [37]. A reduction of these
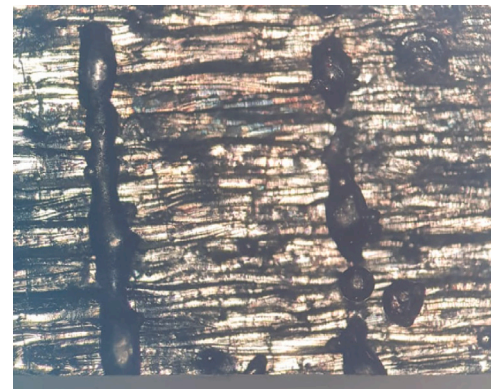

Fig. 6. Top view of the single track experiments seen also in Fig. 5.

defects was sought after in the course of the EU-funded CUSTODIAN [4] project through appropriate beam shaping using MPLC technology. As a result of conducting metallurgical investigations in a preceding study within the CUSTODIAN project [38], it was identified that the defect density increases drastically, when the material is cooled down rapidly from its melted state. More specifically a rapid cooling inside a well-defined temperature range, known as the brittle temperature region (where the alloy's phases coexist in a so-called mushy zone), contributes greatly to crack formation. The nucleation and crystalline growth at different locations inside this region results in a morphology where growing crystals are surrounded by a liquid melt at the grain boundaries. This temperature range usually lies a few hundred degrees below the liquidus temperature. By rapidly cooling the melt, the liquid melt does not have time to back-fill all of the intermittent spaces created by tensile stresses caused by contraction of the material [36].

Following the validation of the simulation model in Section 2.2, a parameter study was carried out in order to obtain appropriate beam
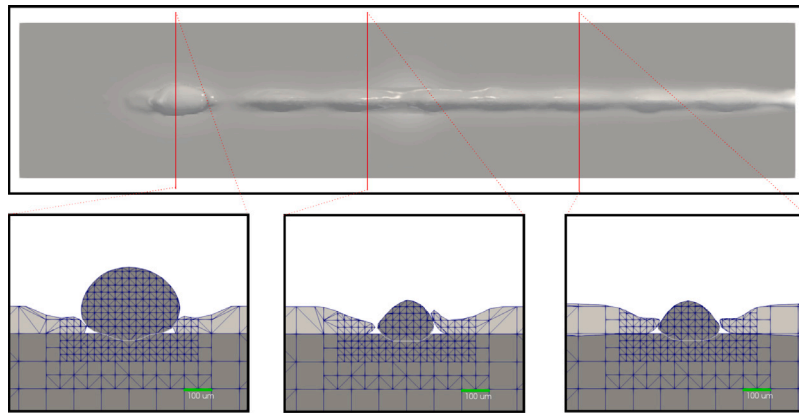
Fig. 7. Single track simulation: Top view and exemplary cross sections with IN713LC, P = 452 W.
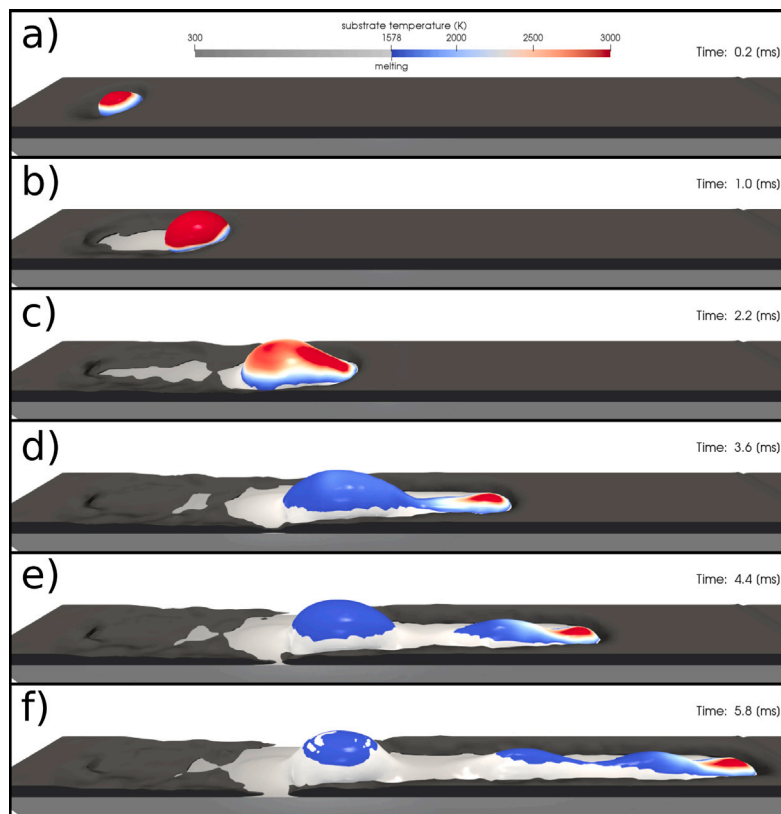

Fig. 8. Single track simulation of PBF-LB/M of IN713LC, P = 452 W: (a)–(c) Formation of first spherical agglomeration. (d)–(f) Formation of subsequent agglomerations.

shapes for a dual beam setup for each of the investigated materials in Section 3.3 and Section 3.4.

3.1. Optimization methodology

In order to avoid micro-structural damage to the final part, an approach to reduce the cooling rates, $\frac{dT}{dt}$, in the most susceptible temperature range, by means of laser beam shaping, was pursued. More details on the calculation of the cooling rates and their usage is presented in Section 3.2.

A secondary goal was to achieve a welded cross section with a high width-to-depth ratio, as this was also found to reduce the probability of cracking. The crack susceptibility is greater in a deep and narrow melt pool [39], because in this case the thermal gradients are oriented parallel to the free surface, where the movement of the material is restricted. In the case of a shallow melt pool, the surface of the mushy

zone can move freely when experiencing tensile stresses and thus help reduce their concentration in the solidified substrate.

The scanning speed in Sections 3.3 and 3.4 is not varied from the value of $v_s = 750\ \frac{\text{mm}}{\text{s}}$ used in Section 2.2 for the validation against experiments.

3.2. Calculation of cooling rates for comparative study

The cooling rates are calculated at run-time at every point (cell-center) where material has previously been molten and its temperature is passing the brittle temperature range [38] during the course of the simulation. To limit the amount of data to be stored, only the maximum value of $\frac{dT}{dt}$ during the entire simulation is stored. Furthermore, to enable a quick quantitative comparison between simulated processes with differing melt pool sizes, the cooling rates are discretized in bins and the volume of material being cooled within these bins, $V(\frac{dT}{dt})$, is
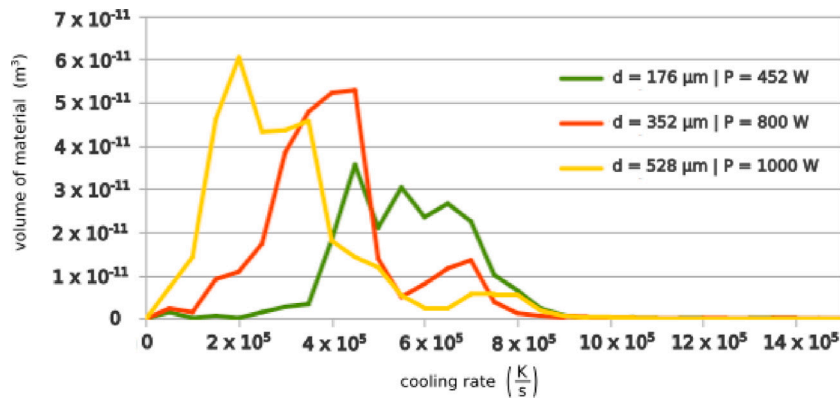
Fig. 9. Cooling rate curves using different primary beam.
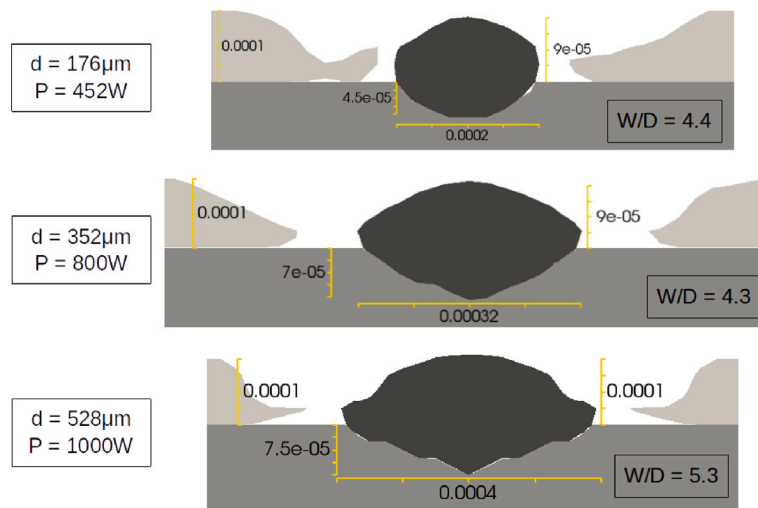

Fig. 10. Cross sections using different primary beams used for width-to-depth ratio (W/D) comparison.

Table 2
Configurations for investigations on primary beam influence on CM247LC.

Spot diameter on work-piece surface d (μm)	Laser power P (W)
176	452
352	800
528	1000

summed up and plotted. The bin size was carefully chosen to find a compromise between spurious data smoothing and noise. The resulting curves are then compared to each other, as is shown for example for different sized laser spots in Fig. 9. A certain beam combination is regarded as superior in terms of cracking susceptibility, if the geometric center of its plot curve is shifted towards the origin of the graphs relative to other process conditions.

3.3. Beam shape optimization on CM247LC

Before adding a secondary beam to the process, the influence of changing primary beam size and power was investigated. Two larger spot sizes were investigated (see Table 2), while adjusting the power to keep the penetration depth similar. The resulting cooling rates in the brittle temperature region from 1523 K to 1673 K [38] were plotted and then compared to the reference condition. This is shown in Fig. 9 and the respective cross sections in Fig. 10.

An investigation of even larger spot sizes was deemed unnecessary due to the limitations in power of real-world laser systems, the inaccuracy introduced by larger spots and the clear trend that was observed. These trends led to the conclusion that larger illuminated areas at similar intensities lead to lower cooling rates and more favorable cross sections (enforced by the condition of keeping the penetration depth similar).

A main strategy followed during CUSTODIAN consists of pre- and/or post-heating the powder and/or substrate to further reduce the risk of solidification crack appearance. Due to the high scanning speeds necessary in PBF-LB/M and the utilization of random scan patterns, there was a need for a beam geometry that is rotationally symmetric. This requirement aimed to avoid the rotation of the laser head, which was beyond the scope of the project.

Several experiments were conducted, which determined that a unidirectional scanning strategy cannot be used and therefore asymmetrical shapes are not possible. As shown in Fig. 11, when employing a unidirectional scanning direction without rotation between layers, noticeable swelling occurs in the topmost layers, leading to an intensified cracking phenomenon. Avoiding rotation between layers leads to a cracking tendency along the build direction. For this reason, the secondary beam was chosen to be circular, concentric to the primary beam and of tophat energy distribution as depicted in Fig. 12.

The pairings of primary and secondary beams are summarized in Table 3. These values resulted from careful evaluation of efficiency and restrictions in form of maximum available power, recyclability of the powder, surface area of the samples, as well as accuracy. After a few
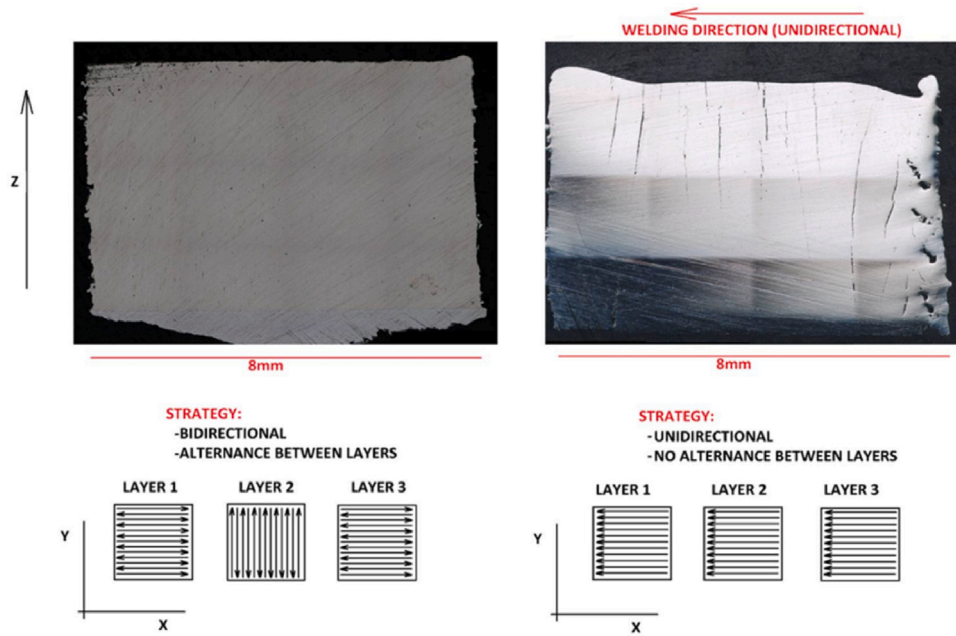
Fig. 11. Cross section analysis of CM247LC processed by different scanning strategies; bidirectional + alternated (LEFT), and unidirectional + no alternance between layers (RIGHT). Process parameters: laser power P = 452 W, scanning velocity v_s = 750 $\frac{mm}{s}$, hatch distance d_h = 100 μm and powder thickness t_p = 50 μm.
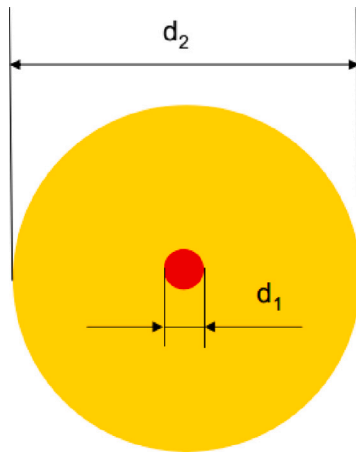
Fig. 12. Sketch of primary and secondary beam combination layout.

Table 3
Parameter combinations investigated on CM247LC (best beam combination highlighted in the last row)

Primary spot diameter on work-piece surface d_1 (μm)	Primary laser beam power P_1 (W)	Secondary spot diameter on work-piece surface d_2 (μm)	Secondary laser beam power P_2 (W)
176	452	5700	3000
176	452	6000	3000
176	452	5700	2800
176	452	5700	2600
176	452	3000	1000
352	800	5400	2300
352	800	5400	2700
528	1000	1000	100
528	1000	2000	400
528	1000	3000	900
528	1000	4000	1600
528	1000	5000	2500
528	**1000**	**4500**	**2500**

test runs, it became evident that a large secondary spot with enough intensity to preheat the powder and substrate, without actually melting the powder, is favorable in terms of avoiding high cooling rates. That is why secondary spots with large radii and higher power than their coupled primary spots were used. The results of the simulations using the aforementioned laser beam pairings are presented in Figs. 13–18, where cooling rate plots and cross sections are shown.

In conclusion, it can be inferred that the size of the secondary beam has an impact on the extent of pre- and post-heating during the process, and it is advisable to select a larger size within the limits of the available power. This increase in energy input results in a larger portion of the melted volume experiencing lower cooling rates, provided that the intensity of the secondary beam is appropriately selected. However, it was found that the influence of the secondary beam, despite requiring more power, is not as pronounced as the size and power of the primary beam.

The optimal beam combination, considering technological and other limitations, that results in reduced cooling rates and an optimized cross sectional shape, is highlighted in bold lettering in Table 3.

3.4. Beam shape optimization on IN713LC

Using the same simulation tool and appropriately changed material properties (see Fig. A.25) a further parameter study has been conducted on the nickel based superalloy IN713LC. Its chemical composition is summarized in Table A.4.

The simulated domain's geometry and meshing, as well as the general laser parameters, remained unchanged, as shown in Table 1 (note the modification in primary beam power to prevent balling in the reference condition).

As this alloy presents comparable material properties to CM247LC, a similar trend in the parameter study was expected, which was validated by simulating the process using one larger primary spot size and
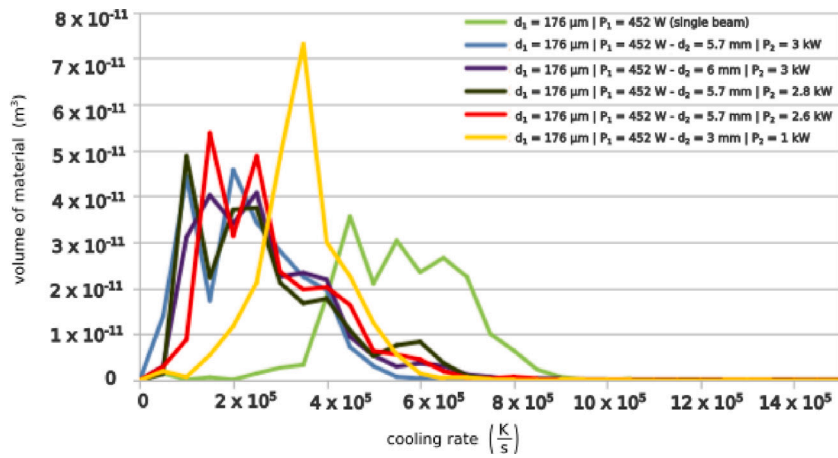
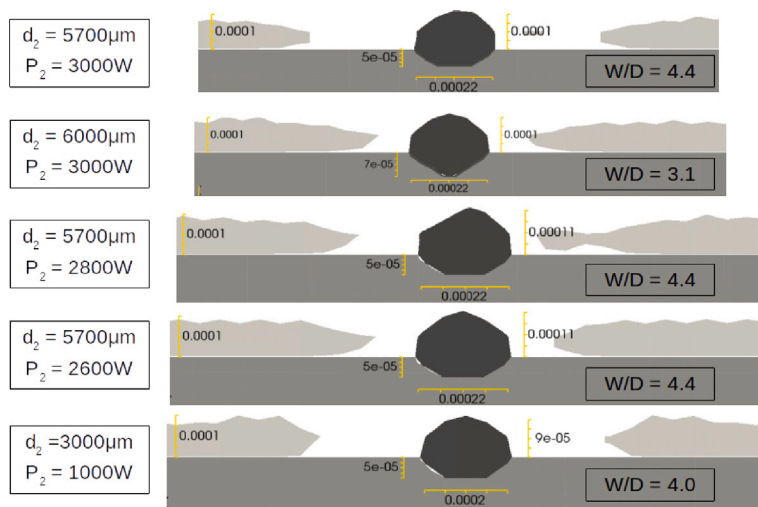**Fig. 13.** Cooling rate curves different secondary beams paired with a 176 μm primary beam.

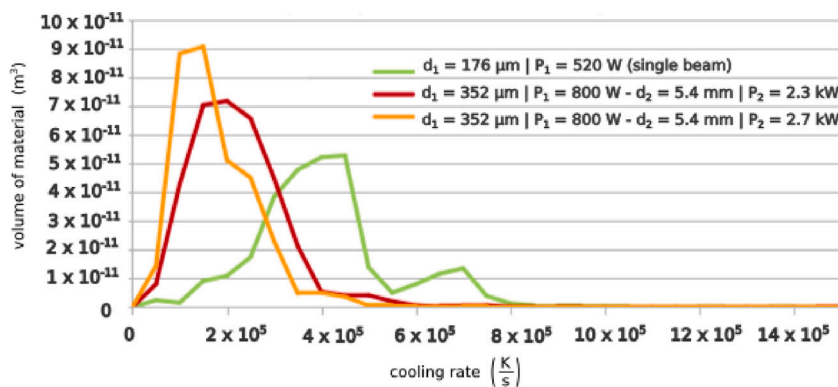**Fig. 14.** Cross sections related to conditions in Fig. 13.

Fig. 15. Cooling rate curves different secondary beams paired with a 352 μm primary beam.

two different secondary beam pairings. The higher power needed for the primary beam however implies less power was available for the secondary beam. The larger primary beam has a spot size of 528 μm and uses 1100 W of power.

The resulting cooling rate plot is shown in comparison to the respective reference condition in Fig. 19. For this material the brittle temperature range is defined from 1213 K to 1571 K [38]. The resulting

cooling rate plots for the tested dual beam configurations can be found in Fig. 20.

In conclusion, the trends for cooling rate reduction and minimizing the risk of solidification cracking remain consistent for IN713LC, similar to CM247LC. The optimal values differ slightly due to a higher primary beam power requirement for IN7LC, as explained in Section 2.2.
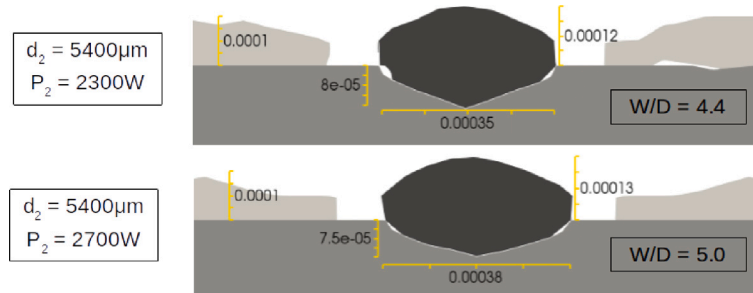
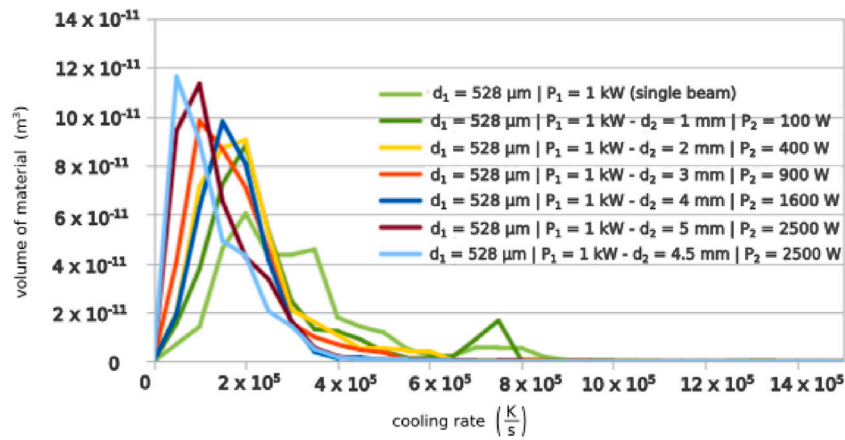**Fig. 16.** Cross sections related to conditions in Fig. 15.

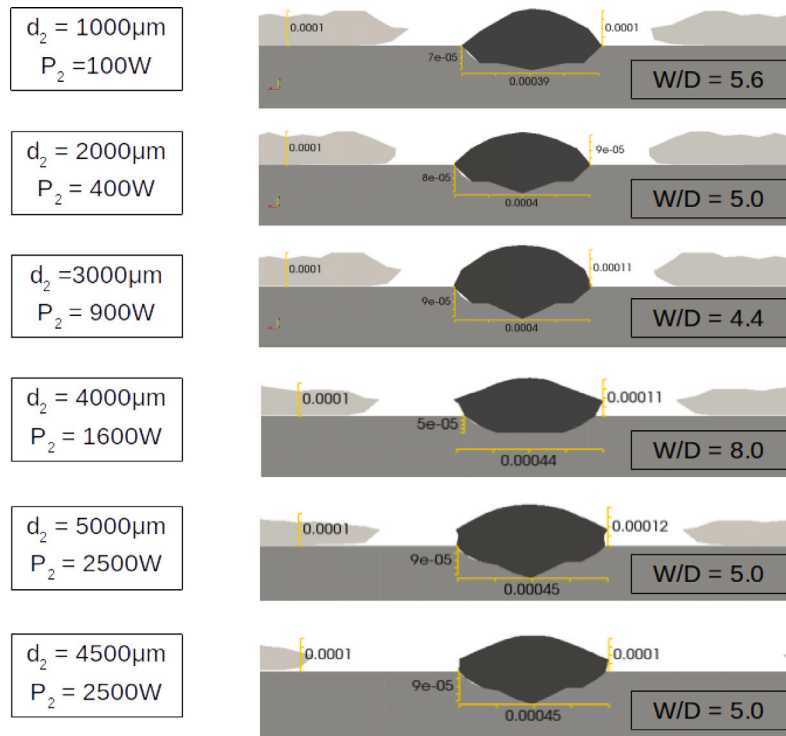**Fig. 17.** Cooling rate curves of different secondary beams paired with a 528 μm primary beam.

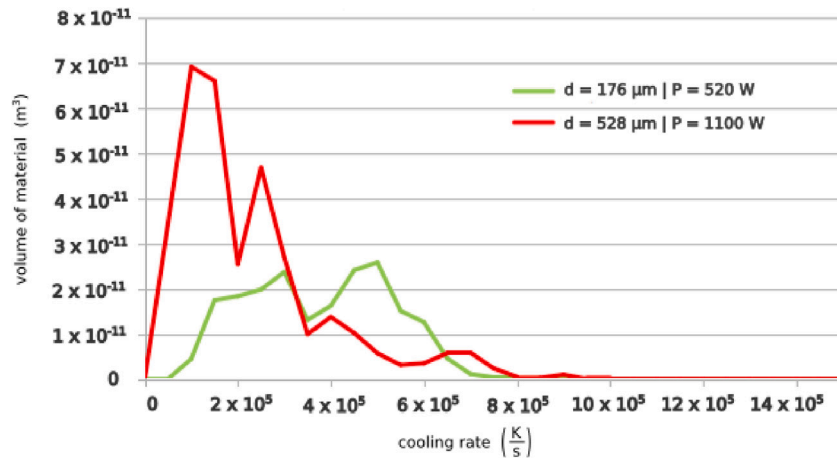**Fig. 18.** Cross sections related to conditions in Fig. 17.

Fig. 19. Cooling rate plot of a larger primary beam compared to the reference condition.
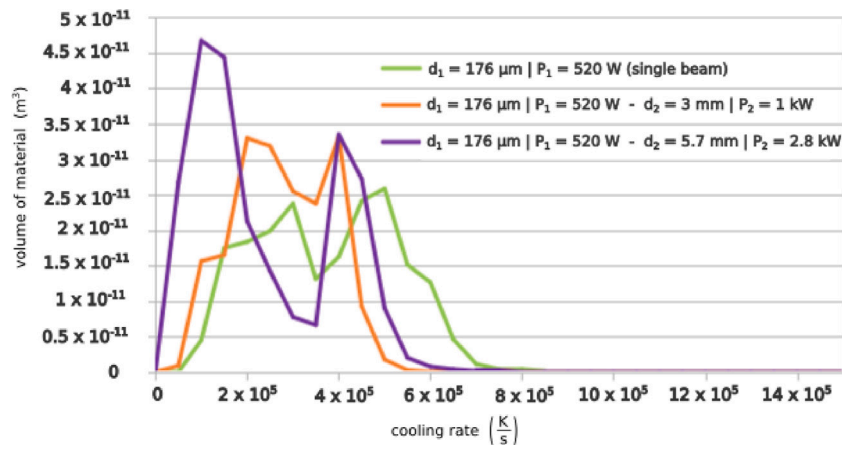

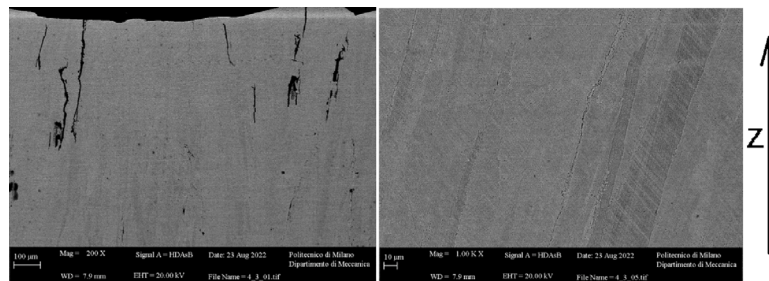**Fig. 20.** Cooling rate plot of selected dual beam configurations.

Fig. 21. IN713LC sample produced by one of the tailored beam shapes.

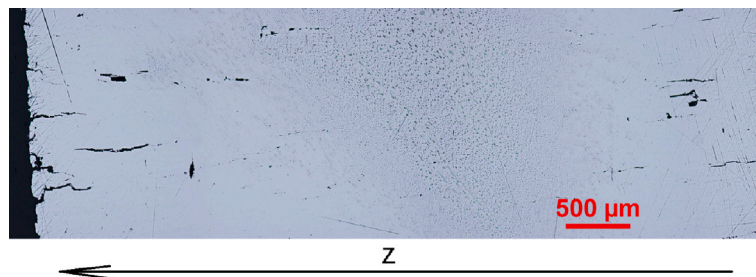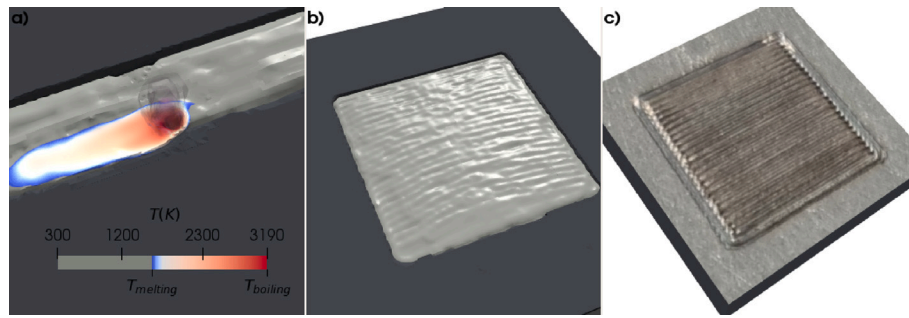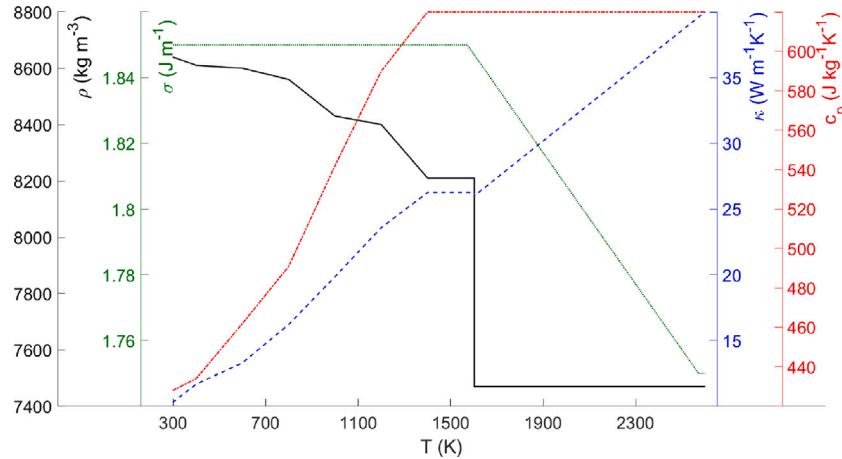**Fig. 22.** CM247LC sample produced by one of the tailored beam shapes.

Fig. 23. Processing of 5 × 5 mm of CM247LC: (a) Melt pool top surface colored by temperature, vapor depression and vapor plume during track 6 of 49. (b) Final, solidified top surface of 5 × 5 mm sample (after 49 scan tracks). (c) Top surface of corresponding experiment.

Fig. A.24. Temperature-dependent values for density, ρ, specific heat capacity, c_p, and thermal conductivity, κ, [32,40] and surface energy, σ [41–43], of CM247LC.

3.5. Validation of the cracking phenomenon improvement through 3D printing tests

In order to verify the optimized results obtained from the simulations, using beam shapes defined within CUSTODIAN, 3D printing tests were carried out at part scale. A custom optical bench (MPLC) was developed and installed in the PBF-LB/M machine, enabling the modification of the beam shapes. This setup was installed and tested in the above mentioned laboratory facilities. A process parameter mapping was carried out over both materials (CM247LC and IN713LC) by varying scanning speed, laser power, line offset, layer height, scanning strategy, and primary and secondary beam power ratio. Cross section were then produced and analyzed. Figs. 21 and 22 display the best results obtained in the process parameter mapping of both materials. However, it was observed that cracks were still evident specifically on the bottom and top areas of the sample. Nevertheless, a fairly dense structure was observed at mid-thickness with the number of cracks greatly reduced in comparison to the material processed under a standard single beam setup. In conclusion, significant improvement in the cracking behavior has been achieved, especially in the mid-part region of the processed samples where large cracks with open faces are less frequent. However, further studies must be conducted to reduce crack formation on the top and bottom areas of the sample. To further decrease crack occurrence, the here-presented methodology should be applied to explore more advanced, asymmetrical beam shapes in subsequent studies, once the limitations regarding laser head rotation are overcome.

4. Outlook: Simulation of multi track process

To demonstrate the suitability of the above-presented simulation model to simulate large-scale processes, processing of a 5 × 5 mm layer of CM247LC consisting of 49 tracks of alternating direction is simulated. The process parameters (velocity, power, powder bed height) are unchanged from those listed in Table 1. Fig. 23 shows the results of this simulation and the corresponding experiment. To the best knowledge of the authors, no process of this scale has ever been simulated taking into account fluid flow phenomena such as evaporation and vapor plume movement and compressible fluid flow. Due to the FVM approach and an adaptive meshing strategy, the simulation was completed within approximately 130 h on an eight core AMD Ryzen 7 2700 CPU. Considering that defects, such as the above-discussed balling defect, are the result of fluid flow phenomena, where effects such as surface tension, evaporation, etc. cannot be neglected, it is important to bring multiphysical models, which are currently at most used for the simulation of single scan tracks, towards the part scale.

5. Conclusion

- A methodology to improve an existing PBF-LB/M process through beam shaping using a passive optical element based on MPLC technology was presented.
- An optimization loop using a multiphysical simulation model to find appropriate beam shape combinations is presented, overcoming the problem of unfeasibility of experiments within the proposed approach.
- The capability of the multiphysical simulation to identify process defects is highlighted at the example of the balling defect, which is identified both in simulation and experiment at insufficient energy input.
- A PBF-LB/M process was optimized with the aim of reducing solidification cracking susceptibility, through the introduction of a secondary, low-intensity heat source aimed at reducing cooling
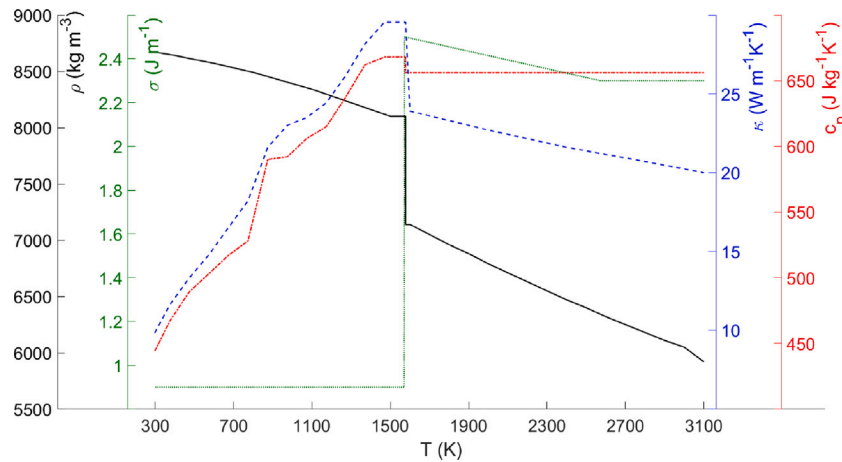
Fig. A.25. Temperature-dependent values for density, ρ [43], specific heat capacity, c_p, thermal conductivity, κ, [44] and surface energy, σ [41–43], of IN713LC.

rates, observing a trend of larger spot sizes leading to a reduced probability of crack formation, mostly at the expense of accuracy.

- The effectiveness of the optimized beam shapes was proven in experiments, where crack density was reduced to near-zero, which was not possible using only a single Gaussian laser beam.
- An outlook over the capabilities of the model in terms of part-scale simulations was presented, reflecting the adaptability, flexibility and efficiency of this generically programmed multiphysical simulation tool to be used for process optimization under industrially relevant conditions.
- The here-presented methodology is especially interesting for industrial application due to the low investment costs required to upgrade an existing process through retrofitting and as no experimental optimization study is needed, with simulations being sufficiently fast to run on a standard desktop computer. Future work should focus on larger parameter spaces regarding the beam shape definitions, including statistical methods to reduce the number of high-fidelity multiphysical simulations to be performed.

CRediT authorship contribution statement

Constantin Zenz: Writing – review & editing, Writing – original draft, Visualization, Validation, Software, Methodology, Investigation, Formal analysis, Data curation. **Michele Buttazzoni:** Writing – review & editing, Writing – original draft, Visualization, Validation, Software, Methodology, Investigation, Formal analysis, Data curation. **Mario Martínez Ceniceros:** Writing – review & editing, Writing – original draft, Visualization, Validation, Methodology, Investigation, Formal analysis. **Rodrigo Gómez Vázquez:** Writing – review & editing, Software, Methodology, Conceptualization. **Jose Ramón Blasco Puchades:** Writing – review & editing, Investigation, Formal analysis, Data curation. **Luis Portolés Griñán:** Writing – review & editing, Supervision, Resources, Project administration, Funding acquisition, Conceptualization. **Andreas Otto:** Writing – review & editing, Supervision, Resources, Project administration, Funding acquisition, Conceptualization.

Declaration of competing interest

The authors declare that they have no known competing financial interests or personal relationships that could have appeared to influence the work reported in this paper.

Data availability

Data will be made available on request.

Table A.4
Chemical composition of investigated alloys [38].

	C	Cr	Co	Mo	W	Ta	Nb	Al	Ti	Hf	Zr	B	Ni
CM247LC	0.07	8.0	9.3	0.5	9.5	3.2		5.6	0.7	1.4	0.010	0.015	bal.
IN713LC	0.05	12.0		4.5			2.0	5.9	0.6		0.1	0.01	bal.

Appendix. Material properties

See Table A.4 and Figs. A.24 and A.25.

References

[1] T. DebRoy, H. Wei, J. Zuback, T. Mukherjee, J. Elmer, J. Milewski, A. Beese, A. Wilson-Heid, A. De, W. Zhang, Additive manufacturing of metallic components – Process, structure and properties, Prog. Mater. Sci. 92 (2018) 112–224, http://dx.doi.org/10.1016/j.pmatsci.2017.10.001.

[2] S. Sing, W. Yeong, Laser powder bed fusion for metal additive manufacturing: perspectives on recent developments, Virtual Phys. Prototyp. 15 (3) (2020) 359–370, http://dx.doi.org/10.1080/17452759.2020.1779999.

[3] T. DebRoy, T. Mukherjee, J. Milewski, J. Elmer, B. Ribic, J. Blecher, W. Zhang, Scientific, technological and economic issues in metal printing and their solutions, Nature Mater. 18 (10) (2019) 1026–1032, http://dx.doi.org/10.1038/s41563-019-0408-2.

[4] URL https://shapeyourlaser.eu.

[5] M. Meunier, A. Otto, R. Gómez Vázquez, J. Arias, R. Fernández, G. Pallier, P. Jian, O. Pinel, G. Labroille, Freeform beam shaping with multi-plane light conversion for 1.07 µ m ultra-high throughput laser-based material macroprocessing, in: Proceedings of ICALEO 2019, Laser Institute of America (LIA), 2019.

[6] M. Buttazzoni, C. Zenz, A. Otto, R.G. Vázquez, G. Liedl, J. Arias, A numerical investigation of laser beam welding of stainless steel sheets with a gap, Appl. Sci. 11 (2021) 2549, http://dx.doi.org/10.3390/app11062549.

[7] H. Wei, T. Mukherjee, W. Zhang, J. Zuback, G. Knapp, A. De, T. DebRoy, Mechanistic models for additive manufacturing of metallic components, Prog. Mater. Sci. 116 (2021) 100703, http://dx.doi.org/10.1016/j.pmatsci.2020.100703.

[8] V.T. Nguyen, A.B. Murphy, G.W. Delaney, S.J. Cummins, P.W. Cleary, P.S. Cook, D.R. Gunasegaram, M.J. Styles, M.D. Sinnott, Progress towards a complete model of metal additive manufacturing, in: Materials Science Forum, Vol. 1016, Trans Tech Publ, 2021, pp. 1031–1038, http://dx.doi.org/10.4028/www.scientific.net/MSF.1016.1031.

[9] R. Cunningham, C. Zhao, N. Parab, C. Kantzos, J. Pauza, K. Fezzaa, T. Sun, A.D. Rollett, Keyhole threshold and morphology in laser melting revealed by ultrahigh-speed x-ray imaging, Science 363 (6429) (2019) 849–852, http://dx.doi.org/10.1126/science.aav4687.

[10] Y. Shu, D. Galles, O.A. Tertuliano, B.A. McWilliams, N. Yang, W. Cai, A.J. Lew, A critical look at the prediction of the temperature field around a laser-induced melt pool on metallic substrates, Sci. Rep. 11 (1) (2021) 12224, http://dx.doi.org/10.1038/s41598-021-91039-z.

[11] M. Geiger, K.-H. Leitz, H. Koch, A. Otto, A 3D transient model of keyhole and melt pool dynamics in laser beam welding applied to the joining of zinc coated sheets, Prod. Eng. Res. Devel. 3 (2009) 127–136, http://dx.doi.org/10.1007/s11740-008-0148-7.

[12] A. Otto, R. Gómez Vázquez, Fluid dynamical simulation of high speed micro welding, J. Laser Appl. 30 (2018) 032411, http://dx.doi.org/10.2351/1.5040652.

[13] A. Otto, R.G.V.U. Hartel, S. Mosbah, Numerical analysis of process dynamics in laser welding of Al and Cu, Proc. CIRP 74 (2018) 691–695, http://dx.doi.org/10.1016/j.procir.2018.08.040.

[14] R.G.V.H. Koch, A. Otto, Multi-physical simulation of laser welding, Physics Procedia 56 (2014) 1334–1342, http://dx.doi.org/10.1016/j.phpro.2014.08.059.

[15] H. Koch, R.G.V.A. Otto, A multiphysical simulation model for laser based manufacturing, in: J. Eberhardsteiner, et al. (Eds.), European Congress on Computational Methods in Applied Sciences and Engineering, ECCOMAS 2012, 2012, pp. 6709–6722.

[16] M. Buttazzoni, Multiphysical Numerical Simulation of Laser Based Additive Manufacturing Processes: Direct Energy Deposition, TU Wien, 2020.

[17] A. Otto, H. Koch, R.G. Vázquez, Z. Lin, B. Hainsey, Multiphysical simulation of ns-laser ablation of multi-material LED-structures, Physics Procedia 56 (2014) 1315–1324, http://dx.doi.org/10.1016/j.phpro.2014.08.057.

[18] S. Tatra, R.G. Vázquez, C. Stiglbrunner, A. Otto, Numerical simulation of laser ablation with short and ultra-short pulses for metals and semiconductors, Physics Procedia 83 (2016) 1339–1346, http://dx.doi.org/10.1016/j.phpro.2016.08.141.

[19] H. Matsumoto, Z. Lin, J.N. Schrauben, J. Kleinert, R.G. Vázquez, M. Buttazzoni, A. Otto, Rapid formation of high aspect ratio through holes in thin glass substrates using an engineered, QCW laser approach, Appl. Phys. A 128 (4) (2022) 1–10, http://dx.doi.org/10.1007/s00339-022-05404-4.

[20] H. Weller, G. Tabor, H. Jasak, C. Fureby, A tensorial approach to computational continuum mechanics using object-oriented techniques, Comput. Phys. 12 (1998) 620–631, http://dx.doi.org/10.1063/1.168744.

[21] S. Deshpande, L. Anumolu, M. Trujillo, Evaluating the performance of the two-phase flow solver interfoam, Comput. Sci. Discov. 5 (2012) 014016, http://dx.doi.org/10.1088/1749-4699/5/1/014016.

[22] A. Otto, H. Koch, R.G. Vázquez, Multiphysical simulation of laser material processing, Physics Procedia 39 (2012) 843–852, http://dx.doi.org/10.1016/j.phpro.2012.10.109.

[23] H. Hügel, T. Graf, Laser in der Fertigung, Vol. 2, Springer, 2009.

[24] V.R. Voller, C. Prakash, A fixed grid numerical modelling methodology for convection-diffusion mushy region phase-change problems, Int. J. Heat Mass Transfer 30 (8) (1987) 1709–1719, http://dx.doi.org/10.1016/0017-9310(87)90317-6.

[25] K.W. Kolasinski, Surface Science: Foundations of Catalysis and Nanoscience, John Wiley & Sons, 2012, http://dx.doi.org/10.1002/9781119941798.

[26] L. Wang, Y. Zhang, W. Yan, Evaporation model for keyhole dynamics during additive manufacturing of metal, Phys. Rev. A 14 (6) (2020) 064039, http://dx.doi.org/10.1103/PhysRevApplied.14.064039.

[27] F. Rösler, D. Brüggemann, Shell-and-tube type latent heat thermal energy storage: numerical analysis and comparison with experiments, Heat Mass Transf. 47 (8) (2011) 1027–1033, http://dx.doi.org/10.1007/s00231-011-0866-9.

[28] M. Ruths, Surface forces, surface tension, and adhesion, in: Q.J. Wang, Y.-W. Chung (Eds.), Encyclopedia of Tribology, Springer US, Boston, MA, 2013, pp. 3435–3443, http://dx.doi.org/10.1007/978-0-387-92897-5_463.

[29] F.C. Álvarez, Improvement of a Lagrangian Approach for the Multi-Physical Simulation of Powder Based Additive Manufacturing Laser Processes, TU Wien, 2019.

[30] H. Chen, Y. Sun, W. Yuan, S. Pang, W. Yan, Y. Shi, A review on discrete element method simulation in laser powder bed fusion additive manufacturing, Chin. J. Mech. Eng. Addit. Manuf. Front. 1 (1) (2022) 100017, http://dx.doi.org/10.1016/j.cjmeam.2022.100017.

[31] S. Sih, J. Barlow, The prediction of the emissivity and ThermalConductivity of powder beds, Particul. Sci. Technol. 22 (2004) 427–440, http://dx.doi.org/10.1080/02726350490501682.

[32] L. Avala, M. Bheema, P. Singh, R. Rai, S. Srivastava, Measurement of thermo physical properties of nickel based superalloys, Int. J. Mech. Eng. Robot. 1 (2013) 108–112.

[33] J. Kruth, L. Froyen, J. Van Vaerenbergh, P. Mercelis, M. Rombouts, B. Lauwers, Selective laser melting of iron-based powder, J. Mater Process. Technol. 149 (2004) 611–622, http://dx.doi.org/10.1016/j.jmatprotec.2003.11.051.

[34] I. Yadroitsev, A. Gusarov, I. Yadroitsava, I. Smurov, Single track formation in selective laser melting of metal powders, J. Mater Process. Technol. 210 (12) (2010) 1624–1631, http://dx.doi.org/10.1016/j.jmatprotec.2010.05.010.

[35] Z. Li, H. Li, J. Yin, Y. Li, Z. Nie, X. Li, D. You, K. Guan, W. Duan, L. Cao, et al., A review of spatter in laser powder bed fusion additive manufacturing: In situ detection, generation, effects, and countermeasures, Micromachines 13 (8) (2022) 1366, http://dx.doi.org/10.3390/mi13081366.

[36] M. Henderson, D. Arrell, R. Larsson, M. Heobel, G. Marchant, Nickel based super-alloy welding practices for industrial gas turbine applications, Sci. Technol. Weld. Join. 9 (1) (2004) 13–21, http://dx.doi.org/10.1179/136217104225017099.

[37] M. Raza, Y.-L. Lo, Experimental investigation into microstructure, mechanical properties, and cracking mechanism of IN713LC processed by laser powder bed fusion, Mater. Sci. Eng. A 819 (2021) 141527, http://dx.doi.org/10.1016/j.msea.2021.141527.

[38] M. Vedani, Handbook on Metallurgical Defects and Their Genesis, Tech. Rep., Politecnico di Milano, 2019.

[39] E. Hallberg, Investigation of Hot Cracking in Additive Manufactured Nickel-Based Superalloys; Process Optimization and Crack Removal with Hot Isostatic Pressing, Chalmers University of Technology, 2018.

[40] M. Rahimian, Physical Simulation of Investment Casting of Mar-M247 Ni-Based Superalloy (Ph.D. thesis), Carlos III University of Madrid, 2015.

[41] P. Sahoo, T. Debroy, M. McNallan, Surface tension of binary metal - Surface active solute systems under conditions relevant to welding metallurgy, Metall. Trans. B 19 (1988) 483–491, http://dx.doi.org/10.1007/BF02657748.

[42] Y. Su, K. Mills, A. Dinsdale, A model to calculate surface tension of commercial alloys, J. Mater. Sci. 40 (2005) 2185–2190, http://dx.doi.org/10.1007/s10853-005-1930-y.

[43] K. Mills, Y. Youssef, Z. Li, Y. Su, Calculation of thermophysical properties of Ni-based superalloys, ISIJ Int. 46 (2006) 623–6321, http://dx.doi.org/10.2355/isijinternational.46.623.

[44] M. Zielińska, M. Yavorska, M. Porêba, J. Sieniawski, Thermal properties of cast nickel based superalloys, Arch. Mater. Sci. Eng. 44 (2010) 35–38.